High-order harmonic spectroscopy for probing intraband and interband dynamics

Gan Wang,[1] Yu-Xuan Chen,[1,2] Mingjie Li,[3,4] and Tao-Yuan Du[1,2,*]
[1] *School of Mathematics and Physics, China University of Geosciences, Wuhan 430074, China*
[2] *State Key Laboratory of Luminescent Materials and Devices, South China University of Technology, Guangzhou 510640, China*
[3] *Department of Applied Physics, The Hong Kong Polytechnic University, Hung Hom, Kowloon, Hong Kong, China*
[4] *Shenzhen Research Institute, The Hong Kong Polytechnic University, Shenzhen, Guangdong 518057, China*

(Received 23 February 2024; accepted 23 May 2024; published 13 June 2024)

Regarding the high-order harmonic generation (HHG) of solids, the intra- and interband contributions have been disputed for over a decade now. The prior scheme in this context has been limited to resolve the temporal HHG profile. In this work we propose that the real-space intra- and intercell dynamics in crystal structure respectively correspond to the reciprocal-space inter- and intraband dynamics. Thus, we utilize the polarization-resolved symmetry of the HHG yield to clarify its dominant term among the inter- and intraband contributions. For simplicity, we necessarily exclude the impact of the propagation effect and therefore take the monolayer MoS_2 as the representative target material. Robustness of this correspondence scheme has been demonstrated by distinguishing the dominant contribution in the parallel HHG spectra. According to the change of the symmetry in the polarization-resolved harmonic yields, in the case of the tuning carrier distribution the transition of the dominant term between intra- and interband contributions has been verified. This work paves an alternative way to resolve the intra- and interband dynamics based on the structural symmetries of the atomic layer materials.

DOI: 10.1103/PhysRevA.109.063511

I. INTRODUCTION

High-order harmonic generation (HHG) is an extreme photon-upconversion process under the highly nonlinear light-matter interactions. Gas HHG was observed more than three decades ago [1,2], and its physical mechanism was clarified by the three-step process [3,4]. This incontrovertible mechanism paves the avenue to generate extremely short light pulses and provides a spectroscopic tool to control and image the laser-induced electron dynamics in matter [5–11]. HHG in solids has attracted much interest as it may have various applications ranging from the novel light sources to the probe of the quasiparticle dynamics in condensed matter [12–19].

Ghimire *et al.* performed the experiment in the mid-infrared (MIR) field and thought that the underlying HHG mechanism is the intraband Bloch oscillations [13,20]. However, Vampa *et al.* experimentally certified that the interband mechanism under the electron-hole recollision is the main source of HHG radiations for MIR driving pulses by adding a weak second-harmonic beam to study the emission process [21]. Furthermore, solid-state HHG experiments were also achieved in the longer wavelength towards the terahertz field, and the intraband mechanism was found to be dominant in this wavelength regime [22–24]. Thus, there are two main mechanisms resulting in HHG of solids that are usually considered. The first one is the intraband Bloch oscillations. The another one is interband polarization, which has much in common with the three-step model used to explain gas HHG.

The most straightforward approach to disentangling intra- and interband dynamics is to use a theory that allows the HHG yields from the intra- and interband contributions to be calculated separately, such as the semiconductor Bloch equations (SBEs). However, the theoretical confirmation of dominant dynamics is also a challenge. For example, one finds that the separation between intra- and interband contributions is gauge dependent under the Bloch-state basis [25]. In addition, one does not know how to choose dephasing time in a physically meaningful way and does not necessarily give a clear answer to the relative dominant contribution between the two mechanisms in the measurable total HHG yields. These issues have been discussed extensively in the past decade and the dispute is not settled yet.

The HHG in bulk and layered materials has been investigated experimentally; however, the theoretical interpretation of the experimental HHG spectra requires carefulness in the SBE simulations. It is important to identify an experimentally observable feature in HHG spectra, which enables the direct differentiation between intra- and interband mechanisms. According to same experiments, the dominant mechanism can be identified by measuring the attosecond chirp in the time-frequency profile [26], but for a specific harmonic order, this way is not applicable. To address these issues, an intrinsic spectral characteristic reflecting the dominant contribution in solid HHG is indispensable.

Essentially, the bulk samples adopted in experimental HHG have a thickness of approximately 200 μm [27,28], in which the radiated harmonic photons will undergo the propagation and self-absorption processes in solid-state medium. Especially for the transmission spectrum, the high-order harmonic signals collected by the spectrometer inevitably include

---

[*] Contact author: duty710@163.com

the impact of propagation and self-absorption [29–31]. For the disputes about the intra- and interband contributions in bulk materials, it is a great challenge to make an agreement between simulation of SBEs and HHG experiment [32–37]. In addition, the relative contribution between intra- and interband dynamics will also be varied by the propagation under various cases. For simplicity and clarity, the atomic monolayer materials will avoid the abovementioned drawback and thus serve as an ideal platform to specify the signature of intra- and interband dynamics in polarization-resolved HHG spectra.

In this work, we uncover the intrinsic signature that the symmetry of the polarization-resolved harmonic yield could directly characterize the dominant contribution in the experimental HHG spectra. To unveil the solid HHG mechanisms, we introduce an intrinsic connection between the real- and k-space perspectives, and we derive a correspondence that the intra- and interband emissions can be demarcated by the translation and rotation symmetries of the crystal structure. This paper is organized as follows. In Sec. II, we present the theoretical methodology. In Sec. III, we systematically discuss the HHG in monolayer MoS_2. We summarize our paper in Sec. IV. Atomic units are used throughout this paper, unless specified otherwise.

II. THEORETICAL METHODOLOGY

A. Electron dynamics correspondence between real and reciprocal spaces

First, we present the reciprocal-space perspective for the electrons in solids driven by laser fields with the vector potential $\mathbf{A}(t)$. Under the single-particle model, the time-dependent Hamiltonian reads $\hat{\mathcal{H}}(t) = [\mathbf{p}+\mathbf{A}(t)]^2/2 + V(\mathbf{r})$, which consists of the field-involved kinetic energy and the crystal potential. The instantaneous eigenstates and eigenvalues of $\hat{\mathcal{H}}(t)$ are denoted as $|n,\boldsymbol{k}\rangle$ and $\varepsilon_n(\boldsymbol{k})$, and the former are the Houston states $\langle \mathbf{r}|n,\boldsymbol{k}\rangle \equiv e^{-i\mathbf{A}(t)\cdot\mathbf{r}}\phi_{nk} = e^{i\boldsymbol{k}\cdot\mathbf{r}}u_{n\boldsymbol{k}}(\mathbf{r})$, labeled by the shifted crystal momentum $\boldsymbol{k}(t) = \mathbf{k}+\mathbf{A}(t)$ and the band index n, where $\mathbf{k}$ is the initial crystal momentum [38–40]. Under the basis of Houston states $|n,\boldsymbol{k}\rangle$, the time-dependent state can be expanded as $|\Psi(t)\rangle = \sum_n \int_{BZ} C_n(\mathbf{k},t)|n,\boldsymbol{k}\rangle dk$, where n, $\mathbf{A}(t)$, and $C_n(\mathbf{k},t)$ are the energy band index, the vector potential defined as $-\int_{-\infty}^{t}\mathbf{F}(t')dt'$, and the time-dependent coefficients, respectively. The field-induced nonlinear current is $\mathbf{J}(t) = \langle\Psi(t)|\hat{\mathbf{v}}|\Psi(t)\rangle$, and the expectation value of velocity operator $\hat{\mathbf{v}} = i[\hat{\mathcal{H}}(t),\mathbf{r}]$.

The gauge covariant form of the coordinate operator is $\mathbf{r} = i\nabla_{\boldsymbol{k}} + \mathcal{A}$ [41]. Here $\nabla_{\boldsymbol{k}} = \delta_{nm}\nabla_{\boldsymbol{k}}\delta(\boldsymbol{k}-\boldsymbol{k}')$ is the gradient operator which acts on all matrix elements to the right. The diagonal and off-diagonal matrix elements of operator $\mathcal{A}$ are the Berry connection $\mathcal{A}_n(\boldsymbol{k})$ and the transition dipole moment $\mathbf{d}_{nm}(\boldsymbol{k})$, respectively. Thus, the total current could be expressed as

$$\mathbf{J}(t) = \sum_n \int_{BZ} \rho^{\mathbf{k}}_{nn} \nabla_{\boldsymbol{k}}\varepsilon_n(\boldsymbol{k})dk + \sum_{n\neq m}\int_{BZ} i\varepsilon_{nm}(\boldsymbol{k})\rho^{\mathbf{k}}_{mn}\mathbf{d}_{nm}(\boldsymbol{k})dk. \tag{1}$$

Here, $\rho^{\mathbf{k}}_{nn}$ (or $\rho^{\mathbf{k}}_{nm}$) are the diagonal (or off-diagonal) elements of the density matrix, related to the coefficients as $\rho^{\mathbf{k}}_{nm} = C_n(\mathbf{k},t)C^*_m(\mathbf{k},t)$. $\varepsilon_{nm}(\boldsymbol{k})$ is the energy difference between bands n and m. The total current consists of the intra- and interband currents. The intraband current is characterized by the diagonal elements of the velocity matrix as $\mathbf{v}_{nn} = \nabla_{\boldsymbol{k}}\varepsilon_n(\boldsymbol{k})$. Furthermore, the interband polarization corresponds to the off-diagonal elements of the velocity matrix as $\mathbf{v}_{nm} = i\varepsilon_{nm}(\boldsymbol{k})\mathbf{d}_{nm}(\boldsymbol{k})$.

Next, we revisit the coordinate operator $\mathbf{r}$ under the real-space perspective, via decomposing this operator as $\mathbf{r} = \mathbf{R} + \mathbf{r}_c$ [41,42]. Here $\mathbf{r}_c$ represents the coordinate within the unit cell with reference to the arbitrary origin of coordinates in the unit cell, while $\mathbf{R}$ denotes the location of lattice sites. Under the Houston state basis $|n,\boldsymbol{k}\rangle$, the matrix elements of $\mathbf{r}$ are

$$\langle m,\boldsymbol{k}'|\mathbf{r}|n,\boldsymbol{k}\rangle = \int_{\mathcal{V}}\phi^*_{m\boldsymbol{k}'}\mathbf{r}\phi_{n\boldsymbol{k}}d\boldsymbol{r}. \tag{2}$$

We expand the integral of Eq. (2) into two characteristic integrals over the unit cells as follows:

$$\begin{aligned}\int_{\mathcal{V}}\phi^*_{m\boldsymbol{k}'}\mathbf{r}\phi_{n\boldsymbol{k}}d^3r &= \sum_{\mathbf{R}_i}\int_{\mathcal{C}} u^*_{m\boldsymbol{k}'}(\mathbf{r}_c+\mathbf{R}_i)u_{n\boldsymbol{k}}e^{i(\boldsymbol{k}-\boldsymbol{k}')\cdot(\mathbf{r}_c+\mathbf{R}_i)}d\mathbf{r}_c\\ &= \underbrace{\sum_{\mathbf{R}_i}\mathbf{R}_i\, e^{i(\boldsymbol{k}-\boldsymbol{k}')\cdot\mathbf{R}_i}\int_{\mathcal{C}} u^*_{m\boldsymbol{k}'}u_{n\boldsymbol{k}}e^{i(\boldsymbol{k}-\boldsymbol{k}')\cdot\mathbf{r}_c}d\mathbf{r}_c}_{\mathrm{X}_{\mathbf{R}}}\\ &\quad+\underbrace{\sum_{\mathbf{R}_i}e^{i(\boldsymbol{k}-\boldsymbol{k}')\cdot\mathbf{R}_i}\int_{\mathcal{C}} u^*_{m\boldsymbol{k}'}u_{n\boldsymbol{k}}\,\mathbf{r}_c\, e^{i(\boldsymbol{k}-\boldsymbol{k}')\cdot\mathbf{r}_c}d\mathbf{r}_c}_{\mathrm{X}_{\mathcal{C}}}.\end{aligned} \tag{3}$$

Here the subscripts $\mathcal{V}$ and $\mathcal{C}$ respectively represent the integrals within the whole sample volume and the unit cell, and $\mathbf{R}_i$ is the location of lattice sites with the site index i. The integral in Eq. (3) is composed of two parts labeled as $\mathrm{X}_{\mathbf{R}}$ and $\mathrm{X}_{\mathcal{C}}$. The structural symmetry of lattice sites is encoded in the term $\mathrm{X}_{\mathbf{R}}$, and $\mathrm{X}_{\mathcal{C}}$ denotes the centroid of the electronic wave packet within unit cells. We further simplify them into

$$\mathrm{X}_{\mathbf{R}} = \delta_{nm}i\nabla_{\boldsymbol{k}'}\delta(\boldsymbol{k}-\boldsymbol{k}'), \tag{4a}$$

$$\mathrm{X}_{\mathcal{C}} = \delta_{nm}\delta(\boldsymbol{k}-\boldsymbol{k}')\mathcal{A}_n(\boldsymbol{k}) + (1-\delta_{nm})\delta(\boldsymbol{k}-\boldsymbol{k}')\mathbf{d}_{mn}(\boldsymbol{k}). \tag{4b}$$

Therefore we can also identify $\mathbf{r} = \delta_{nm}i\nabla_{\boldsymbol{k}}\delta(\boldsymbol{k}-\boldsymbol{k}') + \mathcal{A}$, which is consistent with the expression presented in Blount's work [41]. The Eqs. (4a) and (4b) imply that there is one-to-one correspondence for coordinate operator $\mathbf{r}$ between real- and k-space representations, i.e.,

$$\mathbf{R} = \delta_{nm}i\nabla_{\boldsymbol{k}}\delta(\boldsymbol{k}-\boldsymbol{k}'), \quad \mathbf{r}_c = \mathcal{A}. \tag{5}$$

Thus, the velocity operator in real space can be further rewritten as $\hat{\mathbf{v}} = \hat{\mathbf{v}}_{\text{intercell}} + \hat{\mathbf{v}}_{\text{intracell}}$, where $\hat{\mathbf{v}}_{\text{intercell}} = i[\hat{\mathcal{H}}(t),\mathbf{R}]$ describes the cell-to-cell diffusion of the electronic wave packet, while $\hat{\mathbf{v}}_{\text{intracell}} = i[\hat{\mathcal{H}}(t),\mathbf{r}_c]$ denotes the local oscillation of the electronic wave packet within the unit cell, and this similar dynamics in real space was preliminarily discussed in one-dimensional representation [43]. Considering the spatial features of these two velocity operators, we also call the expectations $\langle\hat{\mathbf{v}}_{\text{intercell}}\rangle$ and $\langle\hat{\mathbf{v}}_{\text{intracell}}\rangle$ as the inter- and intracell velocities, respectively.

It is easy to obtain that $[\mathcal{H}(t),\mathbf{R}]_{n\neq m} = 0$ and $[\mathcal{H}(t),\mathbf{r}_c]_{nn} = 0$; hence, the nondiagonal matrix elements

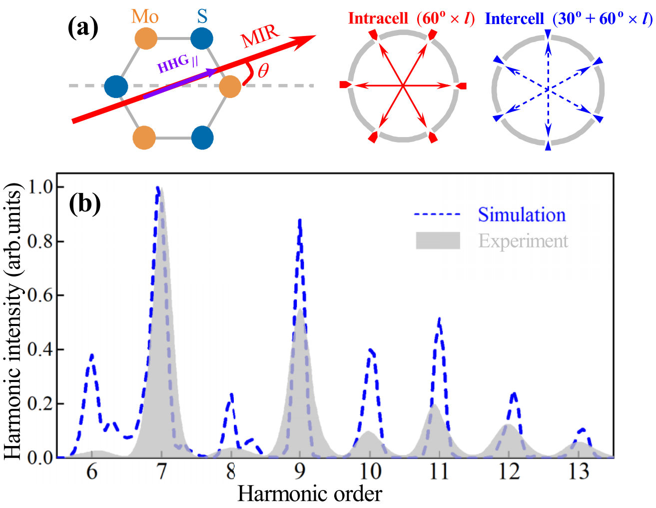

FIG. 1. (a) Top view of the monolayer $\mathrm{MoS_2}$ (leftmost panel) and the angle θ denoting the crystallographic orientation with respect to the MIR laser polarization direction (red arrow). Two right panels respectively show the intracell ($60^\circ \times l$) and intercell ($30^\circ + 60^\circ \times l$) structure symmetries. (b) High-order harmonic spectra obtained from simulation (blue dash curve) and experiment [49] (gray shadow-zone curve). To reproduce the HHG spectrum, the laser wavelength (4130 nm) adopted in the experiment is used in the theoretical simulation.

of $\hat{\mathbf{v}}_{\mathrm{intercell}}$ and the diagonal matrix elements of $\hat{\mathbf{v}}_{\mathrm{intracell}}$ make no contributions to the currents. We can further deduce the matrices of the inter- and intracell velocities as

$$\langle \hat{\mathbf{v}}_{\mathrm{intercell}} \rangle = \sum_{n} i[\mathcal{H}(t), \mathbf{R}]_{nn} = \sum_{n} \mathbf{v}_{nn}, \tag{6a}$$

$$\langle \hat{\mathbf{v}}_{\mathrm{intracell}} \rangle = \sum_{n \neq m} i[\mathcal{H}(t), \mathcal{A}]_{nm} = \sum_{n \neq m} \mathbf{v}_{nm}, \tag{6b}$$

in which n and m denote the indices of energy bands. Consequently, the intra- and interband transition dynamics in k space, which are respectively represented by $\sum_n \mathbf{v}_{nn}$ and $\sum_{n\neq m} \mathbf{v}_{nm}$, correspond one-to-one to the real-space wave-packet dynamics involving $\langle \hat{\mathbf{v}}_{\mathrm{intercell}} \rangle$ and $\langle \hat{\mathbf{v}}_{\mathrm{intracell}} \rangle$. This intrinsic correspondence between the real space and the k space offers a joint and complementary perspective to probe the wave-packet dynamics in the HHG process.

B. Semiconductor Bloch equations

Based on the nearest-neighbor (NN) tight-binding model, the Hamiltonian of the monolayer $\mathrm{MoS_2}$ reads [44,45]

$$\mathcal{H}_0(\mathbf{k}) = \begin{bmatrix} \Delta/2 & h_1 f(\mathbf{k}) \\ h_1 f^*(\mathbf{k}) & -\Delta/2 \end{bmatrix}, \tag{7}$$

where $f(\mathbf{k}) = \exp(i\frac{ak_x}{\sqrt{3}}) + 2\exp(-i\frac{ak_x}{2\sqrt{3}})\cos(\frac{ak_y}{2})$ is determined by the crystal symmetry shown in Fig. 1(a). In addition, the lattice constant a, the band gap Δ, and the NN hopping term h_1 are 5.9 a.u., 1.8 eV, and -0.39 eV, respectively. Diagonalizing the field-free Hamiltonian $\mathcal{H}_0(\mathbf{k})$, one can obtain the energy-band dispersion ε_m. The dipole matrix elements are calculated as $\mathbf{d}_{mn} = i\langle u_{m\mathbf{k}} | \nabla_{\mathbf{k}} | u_{n\mathbf{k}} \rangle$, where $|u_{n\mathbf{k}}\rangle$ is the cell periodic part of the Bloch function. The theoretical simulations are performed by the scheme of SBEs under the Houston representation. The SBE reads

$$\begin{aligned} \partial_t \rho_{mn}^{\mathbf{k}} = {} & -i\varepsilon_{mn}^{\boldsymbol{k}} \rho_{mn}^{\mathbf{k}} - (1-\delta_{mn})\frac{\rho_{mn}^{\mathbf{k}}}{T_2} \\ & - i\mathbf{F}(t) \cdot \sum_f \left[\rho_{mf}^{\mathbf{k}} \mathbf{d}_{fn}^{\boldsymbol{k}} - \mathbf{d}_{mf}^{\boldsymbol{k}} \rho_{fn}^{\mathbf{k}}\right], \end{aligned} \tag{8}$$

which indicates the time-dependent evolution of the electron density $\rho_{mn}^{\mathbf{k}}$. The dephasing time T_2 adopts 5.2 fs [46] and characterizes the relaxation process of the system. The Fermi-Dirac distribution determines the initial electronic population in the valence and conduction bands, described as $\rho_{nn}^{\mathbf{k}} = [\exp(\frac{\varepsilon_n(\mathbf{k})-\mu}{k_B T}) + 1]^{-1}$. T is chosen as the room temperature. The chemical potential μ is 0 eV, corresponding to the top of the valence band, unless specified otherwise. The monolayer $\mathrm{MoS_2}$ is driven by the linearly polarized laser pulses with a Gaussian envelope. In our theoretical simulations, the laser wavelength, full width at half maximum, and intensity are 3.8 μm, ten optical cycles, and 0.6 $\mathrm{TW/cm^2}$, respectively. We numerically solve the time-dependent evolution of the SBEs via the Crank-Nicolson method, and then we obtain the intra- and interband currents as

$$\mathbf{J}_{\mathrm{intra}}(t) = \sum_{\mathbf{k}\in \mathrm{BZ}} \sum_{n} \rho_{nn}^{\mathbf{k}} \nabla_{\boldsymbol{k}} \varepsilon_n(\boldsymbol{k}), \tag{9a}$$

$$\mathbf{J}_{\mathrm{inter}}(t) = \sum_{\mathbf{k}\in \mathrm{BZ}} \sum_{n\neq m} i\varepsilon_{nm}(\boldsymbol{k}) \rho_{mn}^{\mathbf{k}} \mathbf{d}_{nm}(\boldsymbol{k}). \tag{9b}$$

The total current is $\mathbf{J}_{\mathrm{total}}(t) = \mathbf{J}_{\mathrm{inter}}(t) + \mathbf{J}_{\mathrm{intra}}(t)$. Finally, the high-order harmonic spectrum is obtained from the Fourier transform ($\mathcal{FT}$) on the total current and given by

$$I(\omega) \propto \omega^2 |\mathcal{FT}\{\mathbf{J}_{\mathrm{total}}(t)\}|^2. \tag{10}$$

The high-order harmonic spectrum along a certain direction $\hat{\mathbf{n}}$ could be given by $I_{\hat{\mathbf{n}}}(\omega) \propto \omega^2 |\mathcal{FT}\{\mathbf{J}_{\mathrm{total}}(t) \cdot \hat{\mathbf{n}}\}|^2$.

To clarify the role of the anomalous current in the SBEs simulations, we make a semiclassical discussion about the perpendicular high-order harmonic emissions. Under the adiabatic theorem with first-order correction [47], the interband current of Eq. (9b) could be transformed to the anomalous current $j_{\mathrm{anom}} = \mathbf{F}(t) \times \mathbf{\Omega}(\boldsymbol{k})$, where $\mathbf{\Omega}(\boldsymbol{k}) = \nabla_{\boldsymbol{k}} \times \mathcal{A}(\boldsymbol{k})$ and $\mathcal{A}(\boldsymbol{k})$ are the Berry curvature and the Berry connection, respectively. Broken inversion symmetry in the monolayer $\mathrm{MoS_2}$ gives rise to the nonzero Berry curvature around the $\mathbf{K}$ and $\mathbf{K}'$ valleys in the reciprocal space. Considering the fact that interband transition between valence and conduction bands mainly occurs around two valleys [48], thus the anomalous current contributed by the Berry curvature can be simplified as the summation of these two valleys [16,49,50]. Here this anomalous current is given by $J_{\mathrm{anom}}(t) = \int_{\mathrm{BZ}} j_{\mathrm{anom}}(\boldsymbol{k})\delta[\boldsymbol{k} - \mathbf{A}(t) - \mathbf{K}/\mathbf{K}']d\boldsymbol{k}$ and one can finally deduce $J_{\mathrm{anom}} = \mathbf{F}(t)\sum_{\mathbf{K}/\mathbf{K}'} \mathbf{\Omega}[\mathbf{K}/\mathbf{K}' + \mathbf{A}(t)]$ [50]. The time-reversal symmetry $\mathbf{\Omega}(-\mathbf{k}) = -\mathbf{\Omega}(\mathbf{k})$ and the Kramer degeneracy $\mathbf{K}' = -\mathbf{K}$ ensure the relation as $\Omega[\mathbf{K}' + \mathbf{A}(t)] = -\Omega[\mathbf{K} - \mathbf{A}(t)]$. For each type of valley, the time-dependent Berry curvatures around $\mathbf{K}/\mathbf{K}'$ satisfy the $\Omega[\mathbf{K} - \mathbf{A}(t)] = \Omega[\mathbf{K} - \mathcal{R}^{\theta}\mathbf{A}(t)]$, where the $\mathcal{R}^{\theta}$ indicates rotation operation with $\theta = \frac{2\pi}{3}$. Finally, one could obtain

$$J_{\mathrm{anom}}(t) = \mathbf{F}(t)\Delta\mathbf{\Omega}^{\mathbf{K}}(\mathbf{A}(t)), \tag{11}$$

and $\Delta\Omega^{\mathbf{K}}(\mathbf{A}(t)) = \Omega[\mathbf{K}+\mathbf{A}(t)] - \Omega[\mathbf{K}-\mathbf{A}(t)]$ represents the Berry curvature difference between the points $\mathbf{K}+\mathbf{A}(t)$ and $\mathbf{K}-\mathbf{A}(t)$. Hence, the orientation dependence of $\Delta\Omega^{\mathbf{K}}$ determines the anomalous current and subsequently affects the polarization-resolve patterns of the perpendicular high-order harmonic yields.

C. Gauge invariance of intra- and interband HHG

Under the Bloch basis, the separation between intra- and interband currents had been proven to be gauge-dependent physical quantities [25]. In this work we employ the Houston basis to expand the time-dependent states, which are gauge covariant and will give rise to the gauge-independent separation of the intra- and interband currents. The random-gauge time-dependent Hamiltonian is written as $\hat{\mathcal{H}}_g = [\hat{\mathbf{p}} - \mathbf{A}_g(t)]^2/2 + V(\mathbf{r}) + \Phi_g(\mathbf{r},t)$, where $\mathbf{A}_g(t)$ and $\Phi_g(\mathbf{r},t)$ are the vector potential and the scalar potential in the random gauge, labeled as subscript g. The gauge freedom of the electromagnetic field demands the gauge transformations to be satisfied as follows:

$$\begin{aligned} \mathbf{A}_g(t) &\to \mathbf{A}_g(t) + \nabla\Lambda(\mathbf{r},t), \\ \Phi_g(\mathbf{r},t) &\to \Phi_g(\mathbf{r},t) - \partial_t\Lambda(\mathbf{r},t). \end{aligned} \tag{12}$$

Here $\Lambda(\mathbf{r},t)$ is a differentiable real function. The Hamiltonian turns out to be $\hat{\mathcal{H}}' = [\hat{\mathbf{p}} - \mathbf{A}_g(t) - \nabla\Lambda(\mathbf{r},t)]^2/2 + V(\mathbf{r}) + \Phi_g(\mathbf{r},t) - \partial_t\Lambda(\mathbf{r},t)$. The corresponding phase transformation on the wave function, i.e., $|\Psi_g(\mathbf{r},t)\rangle \to |\Psi'(\mathbf{r},t)\rangle = e^{i\Lambda(\mathbf{r},t)}|\Psi_g(\mathbf{r},t)\rangle$, is made to maintain the invariant of the time-dependent Schrödinger equation. Thus, the wave function in the g gauge is related to the velocity-gauge wave function by $|\Psi_g(\mathbf{r},t)\rangle = e^{i\Lambda(\mathbf{r},t)}|\Psi_v(\mathbf{r},t)\rangle$, and the same transformation also holds for the instantaneous eigenstates, indicated as $|n,\boldsymbol{k}\rangle_g = e^{i\Lambda(\mathbf{r},t)}|n,\boldsymbol{k}\rangle_v$. Under these two gauges, the wave functions can be denoted as

$$\begin{aligned} |\Psi_g(\mathbf{r},t)\rangle &= \sum_{n\mathbf{k}} C_n^g(\mathbf{k},t)|n,\boldsymbol{k}\rangle_g, \\ |\Psi_v(\mathbf{r},t)\rangle &= \sum_{n\mathbf{k}} C_n^v(\mathbf{k},t)|n,\boldsymbol{k}\rangle_v. \end{aligned} \tag{13}$$

The relation between wave function coefficients is $C_n^g(\mathbf{k},t) = \sum_{m\mathbf{q}} \langle n,\boldsymbol{k}|_g e^{i\Lambda(\mathbf{r},t)}|m,\boldsymbol{q}\rangle_v C_m^v(\mathbf{q},t)$, where $\langle n,\boldsymbol{k}|_g e^{i\Lambda(\mathbf{r},t)}|m,\boldsymbol{q}\rangle_v = \delta_{mn}\delta(\mathbf{q}-\mathbf{k})$. Thus, we can obtain the coefficients of the adiabatic basis, which are gauge invariant, i.e., $C_n^g(\mathbf{k},t) = C_n^v(\mathbf{k},t)$. Furthermore, the gauge independence of the density matrix elements is also clarified.

As shown in Eq. (9a), the intraband current is composed of the diagonal part of the density matrix and the group-velocity term, both of which are gauge-independent arguments. For the interband current shown in Eq. (9b), the further two arguments on the right-hand side are both gauge independent. The transition dipole elements are gauge invariant and denoted as

$$\begin{aligned} \langle n,\boldsymbol{k}|_g\hat{\mathbf{r}}|m,\boldsymbol{q}\rangle_g &= \langle n,\boldsymbol{k}|_v e^{-i\Lambda(\mathbf{r},t)}\hat{\mathbf{r}}e^{i\Lambda(\mathbf{r},t)}|m,\boldsymbol{q}\rangle_v \\ &= \langle n,\boldsymbol{k}|_v\hat{\mathbf{r}}|m,\boldsymbol{q}\rangle_v. \end{aligned} \tag{14}$$

Hence, the interband current is gauge independent, which means that the results of distinguishing the intra- and interband contributions of HHG under the adiabatic basis are robust and reliable in this work.

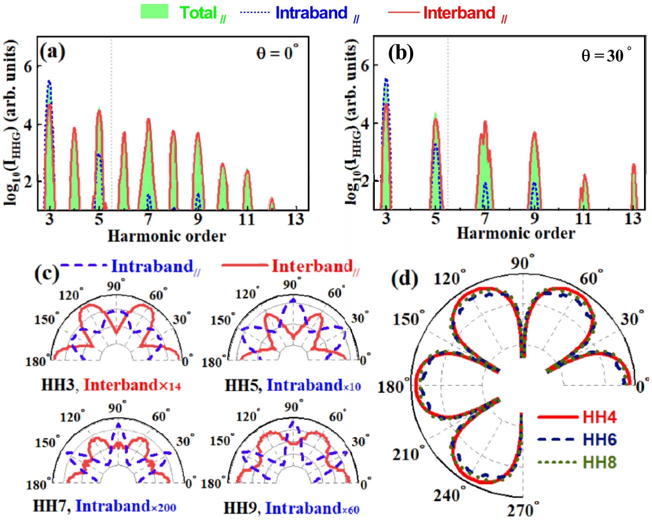

FIG. 2. Parallel harmonic components obtained from the theoretical simulations. In panels (a) and (b) the HHG spectra along two characteristic directions are separated into the intra- and interband contributions. Panels (c) and (d) respectively show the polarization-resolved yield patterns for odd- and even-order harmonics. In panel (c), the intra- and interband contributions have been specified carefully, and the weaker contribution terms have been multiplied by a factor to distinguish the dominate term.

III. RESULTS AND DISCUSSIONS

A. Comparison between experimental and simulated HHG spectra in monolayer MoS_2

For the spectral measurements of HHG experiments in monolayer MoS_2, one usually performs the acquisition of high-harmonic signals along the parallel ($\parallel$) and perpendicular ($\perp$) directions relative to the laser-polarized direction [49]. To make a demonstration, we here theoretically reproduce the experimental high-order harmonic spectrum along the parallel direction of the driving field. As shown in Fig. 1(b), the representative spectrum along $\theta = 0^\circ$ exhibits the 6th to the 13th harmonic of the fundamental field centered at a photon energy of 0.30 eV. In the experimental spectrum (gray-shaded curve) [49], one can observe that the even-order harmonic intensities are much lower than those of odd-order harmonics, and the experimental HHG spectrum characterizes the strongest signal strength at the 7th harmonic. Both of these spectral features have been confirmed by our theoretical high-order harmonic spectrum, as shown in the blue-dashed curve of Fig. 1(b). To make an insight into the observable HHG spectra, in Figs. 2(a) and 2(b) we have separated out the intra- and interband contributions. Excluding the 3rd harmonic, one finds that the interband current dominates both the odd- and even-order harmonics. Contrary to the odd-order harmonics, the even-order harmonics are entirely determined by the interband components.

Figures 2(c) and 2(d) respectively display the odd- and even-order harmonic symmetries of the harmonic yields, which are obtained from the rotation of the linearly polarized laser fields. Note that, for convenience, in Fig. 2(c) the weaker contribution terms have been magnified by a factor.

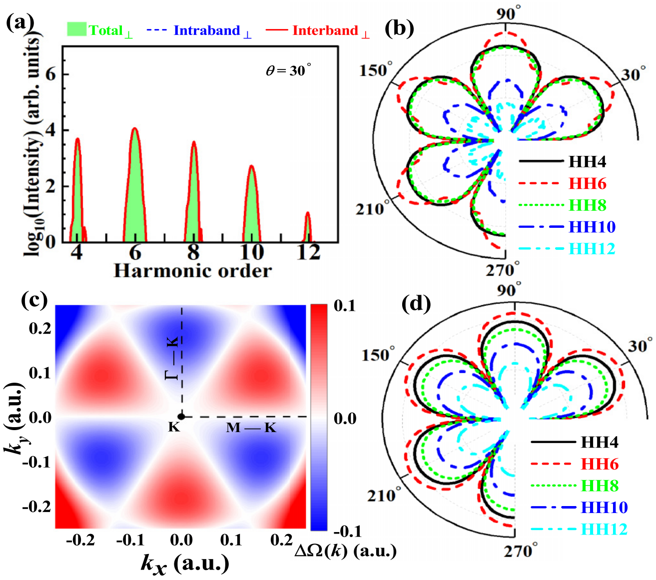

FIG. 3. Perpendicular harmonic components obtained from the theoretical simulations. (a) High-order harmonic spectrum and its contribution separation spectra along $\theta = 30^\circ$. (b) Polarization-resolved patterns of the total harmonics yields. (c) Berry curvature difference $\Delta\Omega^{\mathbf{K}}$ of the valence band around the **K** point. The high symmetry directions of Γ-**K** and **M**-**K** are marked. (d) Polarization-resolved yield patterns obtained from the semiclassical calculations of Eq. (11).

Keeping the negligible intraband contribution in the even-order harmonic in mind, in Fig. 2(d) only the total or interband contribution is shown here. Apart from the 3rd harmonic whose symmetry of the measurable harmonic yields is $\theta = 30^\circ + 60^\circ \times l$, with l being an integer, one can observe that the harmonic maximal yields are along $\theta = 60^\circ \times l$, which is consistent with the experimental measurements [49].

Next we turn to the case where the directions of the fundamental and the harmonic fields are perpendicular. Figures 3(a) and 3(b) respectively exhibit one representative HHG spectrum and its orientation-dependent feature. Similar to the experimental HHG spectra in Ref. [49], only even-order harmonics emerge in the HHG spectra, and their orientation-dependent yield patterns are maximal along $\theta = 30^\circ + 60^\circ \times l$. It is worth emphasizing that in Fig. 3(a) the even-order harmonic spectrum of the perpendicular component is also entirely dominated by interband contributions. To comprehend the perpendicular even-order component, we resort to the anomalous current derived from the Berry curvature $\Delta\Omega$. One observes that the maximal values of $\Delta\Omega^{\mathbf{K}}$ are along the direction of $\theta = 30^\circ + 60^\circ \times l$, as shown in Fig. 3(c). Based on $J_{\text{anom}}(t)$ in Eq. (11), we calculate the perpendicular harmonic components from $\Delta\Omega^{\mathbf{K}}$. The calculated HHG patterns are presented in Fig. 3(d) and reach a great agreement with the SBEs' patterns in Fig. 3(b).

We have reproduced the parallel and perpendicular harmonic components emerging in the HHG experiments of the monolayer MoS_2, and their patterns of the anisotropic harmonic yields have been verified.

B. Correspondence between the polarization-resolved symmetry of the measurable total HHG yields and the dominant contribution term

Several studies have discussed the real-space perspective of electron dynamics under Wannier representation, which is dual to the k-space dynamics [51,52]. However, Wannierization reduces the electron dynamics to an intercell electron hopping, in which the intracell electron transport is lost. Nevertheless, several works have clarified the significant role of the intracell electron dynamics [53,54]. Considering the fact that the inter- and intracell dynamics can be reflected by the symmetries of the crystal structure, the correspondence deduced in Sec. II A provides an ingenious avenue to discern the dominant mechanism between intra- and interband contributions. In fact, the chemical bonds describe the distribution of valence electrons among lattice sites. When the crystalline materials are irradiated by the linearly polarized laser fields, electronic migration or oscillation tends to take place along the intracell directions in which atoms form bonds [55,56], thereby giving rise to interband HHG. In addition, the laser-driven electronic wave packet is also inclined to transport between the adjacent unit cells, known as intercell dynamics that leads to the intraband emissions of HHG. For simplicity, we here designate the polarization-resolved yield patterns of the intra- and intercell HHG as the intra- and intercell symmetries.

Before one straightforwardly adopts the intra- and intercell symmetries to identify the inter- and intraband mechanisms, one should emphasize that the Wigner-Seitz cell is chosen as the primitive cell. Furthermore, considering the anomalous velocity of the electronic wave packet deviates from the direction of the driving laser fields, the correspondence between the reciprocal space and the real space is inapplicable for the perpendicular harmonic components. Next we consider the yield patterns of the parallel harmonic components and unravel their underlying intra- and interband signatures from the perspective of inter- and intracell symmetries.

In the right two panels of Fig. 1(a), $\theta = 30^\circ + 60^\circ \times l$ and $\theta = 60^\circ \times l$ are inter- and intracell symmetries, respectively. Based on the mentioned correspondence shown in Sec. II A, in Figs. 2(a) and 2(b) one could predict that the interband mechanism dominates the all high-harmonic orders except for the 3rd harmonic determined by intraband mechanism. To verify the predictions of the intra- and interband mechanisms, in Figs. 2(c) and 2(d) we separate the intra- and interband contributions for two representative cases. In Figs. 2(c) and 2(d), one can also observe that the 3rd harmonic is dominated by the intraband current, but all the other harmonics are contributed by the interband current. To exclude the impact of the dephasing time, Figs. 4(a) and 4(b) show the HHG spectra under various dephasing times, in which their intra- and interband contributions have also been separate. In Figs. 4(a) and 4(b), one can see that the relative contributions between the intra- and interband currents are totally consistent with those in Figs. 2(c) and 2(d). Note that the separation of intra- and interband contributions is to illustrate the validity of our proposal. Our proposal is based on the polarization-resolved symmetry of the measurable total HHG yield. Finally, one can conclude that the proposal of fingerprint identification

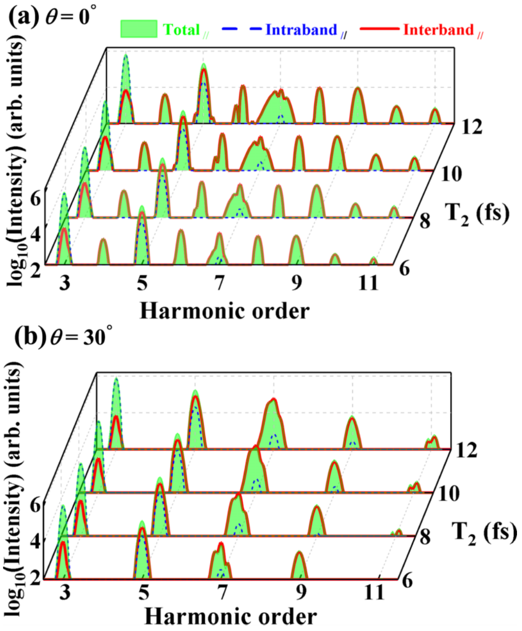

FIG. 4. Impact of the dephasing time T_2 on the intra- and interband contributions. Parallel high-order harmonic spectra varying with T_2 along two characteristic directions (a) $\theta = 0^\circ$ and (b) $\theta = 30^\circ$.

can be effectively used to recognize the intra- or interband mechanism in the HHG process.

C. Transition of the dominant mechanism

Proposal of the fingerprint identification could also predict the mechanism transition between intra- and interband contributions. The HHG process in experiments would be controlled by the doping or depletion of the carriers [57–59]. In Figs. 5(a1) and 5(b1), we illustrate two schematic diagrams with different chemical potentials μ. For the cases with chemical potentials $\mu = 0$ and -0.24 eV, Fig. 5(c) exhibits the polarization-resolved yield pattern of the 5th harmonic. According to the rule that the intracell ($60^\circ \times l$) and intercell ($30^\circ + 60^\circ \times l$) symmetries respectively correspond to the dominant contributions of inter- and intraband currents, in Fig. 5(c) one could predict that the dominant mechanism has been changed from the interband contribution (red solid pattern) into the intraband contribution (blue dash pattern). In Figs. 5(a2) and 5(a3) and Figs. 5(b2) and 5(b3), the separated HHG spectra along two characteristic directions ($\theta = 0^\circ$ and 30°) show that the inter- and intraband currents respectively determine the 5th harmonic emissions in the cases $\mu = 0$ and -0.24 eV, which reach a great agreement with the predicted results via the fingerprint identification.

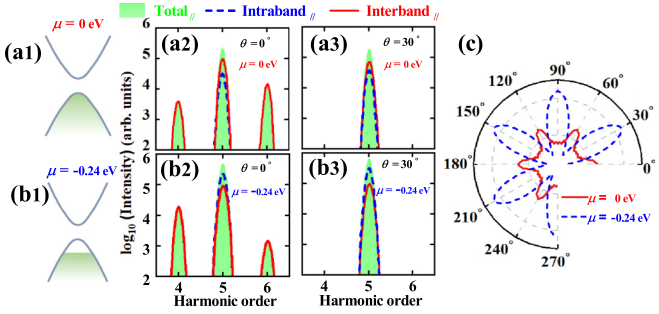

FIG. 5. Transition of the dominant contribution currents under the tuning chemical potential μ. Schematic diagrams for $\mu = 0$ eV (a1) and $\mu = -0.24$ eV (b1). Parallel high-order harmonic spectra along two characteristic directions $\theta = 0^\circ$ and 30° respectively present in panels (a2) or (b2) and panels (a3) or (b3). (c) Polarization-resolved patterns of the 5th harmonic under two chemical potentials.

IV. CONCLUSIONS

In summary, the electronic wave-packet dynamics can be decomposed into the local oscillation within the unit cell and the diffusion among various unit cells, which are called s intra- and intercell dynamics, respectively. According to the characteristics of the wave-packet dynamics, we deduce a correspondence that the intra- and intercell dynamics in real space respectively characterize the inter- and intraband currents in reciprocal space. The spectroscopic symmetries have been obtained from the polarization-resolved measurable HHG spectra via rotating the crystal angle with respect to the polarization direction of the laser fields. Considering the fact that the parallel components of HHG spectra reflect the electronic dynamics along the laser-driving direction, we regard their polarization-resolved symmetries as fingerprints to compare with the intra- and intercell symmetries in the crystal structure, distinguishing the dominant mechanism of high-order harmonic emission in the HHG spectra of monolayer MoS_2.

A detailed recipe can be summarized as follows. First, one chooses the Wigner-Seitz cell as the primitive cell of the crystalline structure. Then, the intra- and intercell symmetries of the crystalline structure can be clearly and uniquely defined. Finally, one can compare the symmetry of the polarization-resolved yield of the given harmonic order with the defined intra- or intercell symmetry to confirm its inter- or intraband dominant mechanism.

Beyond the scheme of the attosecond chirp distinguishing the dominate mechanism [26], in this work we introduce an alternative proposal that the HHG mechanism can be clarified by the intra- and intercell symmetries in the crystal structure. Note that our proposal is more suitable to the cases excluding the intricate propagation effect. By distinguishing the intra- and interband mechanisms in the carrier's doping or depletion solids, our work provides a promising way to enhance and optimize the attosecond light source from the solid-state HHG.

ACKNOWLEDGMENTS

This work was supported by the Natural Science Foundation of Hubei Province China (Grant No. 2023AFB613), the Fundamental Research Funds for the Central Universities, the China University of Geosciences (Wuhan) under Grant No. G1323523064, and the Open Fund of the State Key Laboratory of Luminescent Materials and Devices (South China University of Technology). M.L. acknowledges the financial support from the Research Grant Council of Hong Kong (Projects No. PolyU 25301522 and No. PolyU 15301323) and the National Natural Science Foundation of China (Grant No. 22373081). T.-Y.D. thanks Prof. P. Földi for helpful discussions.

[1] A. McPherson, G. Gibson, H. Jara, U. Johann, T. S. Luk, I. A. McIntyre, K. Boyer, and C. K. Rhodes, J. Opt. Soc. Am. B **4**, 595 (1987).
[2] M. Ferray, A. L'Huillier, X. F. Li, L. A. Lompre, G. Mainfray, and C. Manus, J. Phys. B: At., Mol. Opt. Phys. **21**, L31 (1988).
[3] P. B. Corkum, Phys. Rev. Lett. **71**, 1994 (1993).
[4] M. Lewenstein, P. Balcou, M. Y. Ivanov, A. L'Huillier, and P. B. Corkum, Phys. Rev. A **49**, 2117 (1994).
[5] T. Brabec and F. Krausz, Rev. Mod. Phys. **72**, 545 (2000).
[6] T.-Y. Du, Phys. Rev. A **104**, 063110 (2021).
[7] F. Krausz and M. Ivanov, Rev. Mod. Phys. **81**, 163 (2009).
[8] A. J. Uzan-Narovlansky, Á. Jiménez-Galán, G. Orenstein *et al.*, Nat. Photon. **16**, 428 (2022).
[9] E. Goulielmakis, Z.-H. Loh, A. Wirth, R. Santra, N. Rohringer, V. S. Yakovlev, S. Zherebtsov, T. Pfeifer, A. M. Azzeer, M. F. Kling, S. R. Leone, and F. Krausz, Nature (London) **466**, 739 (2010).
[10] T.-Y. Du and C. Ma, Phys. Rev. A **105**, 053125 (2022).
[11] Y.-X. Chen, G. Wang, M. Li, and T.-Y. Du, Opt. Express **32**, 14940 (2024).
[12] E. Goulielmakis and T. Brabec, Nat. Photon. **16**, 411 (2022).
[13] S. Ghimire, A. D. DiChiara, E. Sistrunk, P. Agostini, L. F. DiMauro, and D. A. Reis, Nat. Phys. **7**, 138 (2011).
[14] M. Borsch, C. P. Schmid, L. Weigl, S. Schlauderer, N. Hofmann, C. Lange, J. T. Steiner, S. W. Koch, R. Huber, and M. Kira, Science **370**, 1204 (2020).
[15] H. Lakhotia, H. Y. Kim, M. Zhan, S. Hu, S. Meng, and E. Goulielmakis, Nature (London) **583**, 55 (2020).
[16] T. T. Luu and H. Wörner, Nat. Commun. **9**, 916 (2018).
[17] L. Yue and M. B. Gaarde, Phys. Rev. Lett. **130**, 166903 (2023).
[18] K. Huang and T.-Y. Du, Phys. Rev. B **108**, 155125 (2023).
[19] R. Zuo, A. Trautmann, G. Wang, W.-R. Hannes, S. Yang, X. Song, T. Meier, M. Ciappina, H. T. Duc, and W. Yang, Ultrafast Sci. **2021**, 9861923 (2021).
[20] S. Ghimire, A. D. DiChiara, E. Sistrunk, U. B. Szafruga, P. Agostini, L. F. DiMauro, and D. A. Reis, Phys. Rev. Lett. **107**, 167407 (2011).
[21] G. Vampa, T. J. Hammond, N. Thiré, B. E. Schmidt, F. Légaré, C. R. McDonald, T. Brabec, and P. B. Corkum, Nature (London) **522**, 462 (2015).
[22] B. Zaks, R. B. Liu, and M. S. Sherwin, Nature (London) **483**, 580 (2012).
[23] O. Schubert, M. Hohenleutner, F. Langer, B. Urbanek, C. Lange, U. Huttner, D. Golde, T. Meier, M. Kira, S. W. Koch, and R. Huber, Nat. Photon. **8**, 119 (2014).
[24] P. D. Keathley, S. V. B. Jensen, M. Yeung, M. R. Bionta, and L. B. Madsen, Phys. Rev. B **107**, 054302 (2023).
[25] P. Földi, Phys. Rev. B **96**, 035112 (2017).
[26] M. Garg, M. Zhan, T. T. Luu, H. Lakhotia, T. Klostermann, A. Guggenmos, and E. Goulielmakis, Nature (London) **538**, 359 (2016).
[27] J. Lu, E. F. Cunningham, Y. S. You, D. A. Reis, and S. Ghimire, Nat. Photon. **13**, 96 (2019).
[28] Y. S. You and M. Wu *et al.*, Opt. Lett. **42**, 1816 (2017).
[29] G. Vampa, Y. S. You, H. Liu, S. Ghimire, and D. A. Reis, Opt. Express **26**, 12210 (2018).
[30] A. Korobenko, T. J. Hammond, C. Zhang, A. Yu. Naumov, D. M. Villeneuve, and P. B. Corkum, Opt. Express **27**, 32630 (2019).
[31] P. Xia, C. Kim, F. Lu, T. Kanai, H. Akiyama, J. Itatani, and N. Ishii, Opt. Express **26**, 29393 (2018).
[32] S. Ghimire, A. D. DiChiara, E. Sistrunk, G. Ndabashimiye, U. B. Szafruga, A. Mohammad, P. Agostini, L. F. DiMauro, and D. A. Reis, Phys. Rev. A **85**, 043836 (2012).
[33] I. Kilen, M. Kolesik, J. Hader, J. V. Moloney, U. Huttner, M. K. Hagen, and S. W. Koch, Phys. Rev. Lett. **125**, 083901 (2020).
[34] Y. Lang, Z. Peng, J. Liu, Z. Zhao, and S. Ghimire, Phys. Rev. Lett. **129**, 167402 (2022).
[35] M. Wu, Y. You, S. Ghimire, D. A. Reis, D. A. Browne, K. J. Schafer, and M. B. Gaarde, Phys. Rev. A **96**, 063412 (2017).
[36] T.-Y. Du, Opt. Lett. **46**, 2007 (2021).
[37] Y. Zhang, M. Zhang, W. Yang, H. Yu, M. S. Si, S. Xue, and H. Du, Phys. Rev. A **108**, 043508 (2023).
[38] W. V. Houston, Phys. Rev. **57**, 184 (1940).
[39] J. B. Krieger and G. J. Iafrate, Phys. Rev. B **33**, 5494 (1986).
[40] L. Yue and M. B. Gaarde, J. Opt. Soc. Am. B **39**, 535 (2022).
[41] E. I. Blount, Solid State Phys. **13**, 305 (1962).
[42] E. N. Adams and E. I. Blount, J. Phys. Chem. Solids **10**, 286 (1959).
[43] T.-Y. Du, X.-H. Huang, and X.-B. Bian, Phys. Rev. A **97**, 013403 (2018).
[44] Y. Lee, D. Kim, D. E. Kim, and A. Chacón, Symmetry **13**, 2403 (2021).
[45] G.-B. Liu, W.-Y. Shan, Y. Yao, W. Yao, and D. Xiao, Phys. Rev. B **88**, 085433 (2013).
[46] G. Wang and T.-Y. Du, Phys. Rev. A **103**, 063109 (2021).
[47] D. Xiao, M. C. Chang, and Q. Niu, Rev. Mod. Phys. **82**, 1959 (2010).
[48] D. Xiao, W. Yao, and Q. Niu, Phys. Rev. Lett. **99**, 236809 (2007).
[49] H. Liu, Y. Li, Y. S. You, S. Ghimire, T. F. Heinz, and D. A. Reis, Nat. Phys. **13**, 262 (2017).
[50] Z. Lou, Y. Zheng, C. Liu, Z. Zeng, R. Li, and Z. Xu, Opt. Express **29**, 37809 (2021).
[51] A. M. Parks, G. Ernotte, A. Thorpe, C. R. McDonald, P. B. Corkum, M. Taucer, and T. Brabec, Optica **7**, 1764 (2020).
[52] F. Catoire, H. Bachau, Z. Wang, C. Blaga, P. Agostini, and L. F. DiMauro, Phys. Rev. Lett. **121**, 143902 (2018).
[53] S. Kitamura, N. Nagaosa, and T. Morimoto, Commun. Phys. **3**, 63 (2020).
[54] N. Nagaosa and T. Morimoto, Adv. Mater. **29**, 1603345 (2017).
[55] Y. You, D. Reis, and S. Ghimire, Nat. Phys. **13**, 345 (2017).
[56] F. Langer, M. Hohenleutner, U. Huttner, S. W. Koch, M. Kira, and R. Huber, Nat. Photon. **11**, 227 (2017).
[57] Z. Wang, H. Park, Y. H. Lai, J. Xu, C. I. Blaga, F. Yang, P. Agostini, and L. F. DiMauro, Nat. Commun. **8**, 1686 (2017).
[58] H. Nishidome, K. Nagai, K. Uchida, Y. Ichinose, Y. Yomogida, Y. Miyata, K. Tanaka, and K. Yanagi, Nano Lett. **20**, 6215 (2020).
[59] C. Heide, Y. Kobayashi, A. C. Johnson, F. Liu, T. F. Heinz, D. A. Reis, and S. Ghimire, Optica **9**, 512 (2022).